



OPEN Disaster-causing mechanism and control technology of interlayer rock breakage in gently inclined close distance coal seams mining

Xiaoqian Yuchi¹✉, Xuanhong Du¹, Pan Shu¹, Lan Yu¹, Wulin Lei¹, Wenhua Yang² & Ze Zhang³

Aiming at the complex issue of dynamic disasters induced by hard rock layers fracture during the mining of gently inclined close distance coal seams, this study employs an integrated approach combining numerical simulation, microseismic monitoring, and mechanical analysis to investigate the fracture evolution process of hard rock layers under the influence of an inverted trapezoidal overburden. A cantilever beam structural model of interlayer rock layers was established, from which the deflection curve and rotation angle equation at the critical fracture state were derived. The elastic energy released upon fracture of the cantilever beam was quantified. Furthermore, by considering the characteristics of the overburden above residual coal pillars, the interplay among the total energy released during interlayer rock fracture, the strength of the cantilever structure, and the inverted trapezoidal overburden load was elucidated. Specifically, a heavier inverted trapezoidal load increases the disaster-induced energy applied to the cantilever structure, a longer cantilever beam accumulates greater elastic energy, and a stiffer beam structure can accumulate more energy. The interaction between these three factors makes it easy to induce strong mining pressure when the hard rock layers break during close distance coal seam mining. Accordingly, combined prevention measures involving water injection softening and blasting roof cutting were proposed to mitigate dynamic hazards and ensure safe mine production.

Keywords Close distance coal seams, Hard rock layers, Microseismic monitoring, Cantilever beam, Blasting roof cutting

Reasonable and effective utilization of coal resources is highly effective in reducing carbon emissions, achieving carbon peak, and promoting stable energy supply^{1–3}. In high-quality coal fields in China, there are often more than one coal seam that can be mined within the zone. How to fully recover all the recoverable coal seams while ensuring safety support is a major help to improve coal utilization efficiency^{4–6}. However, in the face of extremely complex geological problems such as rock bursts and high permeability of CH₄ or coalbed methane, layered mining often presents many technical challenges^{7–9}, especially the instability of hard strata between close range coal seams, which is one of the key factors inducing dynamic disasters^{10–12}. In addition, close range coal seam mining will cause multiple mining disturbances to the overlying strata in the same area¹³, and the structural characteristics inside the overburden will gradually deteriorate under the disturbance. The extension of primary fractures and the increase in the number of associated fractures will ultimately result in local instability and fracture of the overburden¹⁴, release of elastic energy from overlying rock aggregation to form mining pressure manifestation, spatiotemporal displacement of rock layers, and structural distortion on site^{15–17}.

In this context, extensive research has been conducted on the structural evolution of overburden in thick coal seams, including mechanisms of instability and corresponding monitoring and early warning systems. These studies have addressed significant challenges under specific geological conditions. For instance, Lai et al.^{18–20} conducted similar simulation experiments on the “Acoustic - Thermal” evolution characteristics to address the problem of dynamic fracture of hard rock columns between steeply inclined and thick coal seams. Their work revealed the disaster mechanism induced by mining stress distortion and contributed to the development of a roof control strategy for such mining conditions. Yu et al.^{21,22} examined the geological characteristics of

¹School of New Energy, Longdong University, Qingyang, Gansu 745000, People’s Republic of China. ²College of Energy Engineering, Xi’an University of Science and Technology, Xi’an 710054, People’s Republic of China. ³Shaanxi Energy Investment Co., Ltd. Coal Industry Branch, Xi’an 710000, People’s Republic of China. ✉email: 13484519960@163.com

alternating thick coal seams and hard roofs in multiple mining areas in Bangladesh, proposing a layered and staggered mining layout method to prevent disasters in stratified overburden mining. Zhang et al.^{23,24} employed various research methods to establish mechanical models for safe multi-seam mining under thick igneous rocks, analyzing the disaster mechanism caused by fracture instability and crack propagation characteristics, ultimately proposing a backfill mining-based control technique. Deng et al.²⁵ studied overburden fracture height during layered mining in the Gonggezhiyong Coal Mine using ABAQUS simulations and field monitoring, establishing a linear relationship between fracture height and extracted seam thickness, thereby optimizing the mining method. Huang et al.^{26–28} focused on water conservation mining in the Yushen mining area, using physical simulations to analyze fracture evolution and interlayer rock stability in shallow-buried thick coal seams, and proposed pillar layout distances along with water-preservation measures. Peng et al.²⁹ based on elastoplastic theory and numerical simulation, identified a linear relationship between middling pillar width and stope offset in close-distance seams, exploring stress transmission through pillars into the floor and clarifying stress distribution between lower stopes and pillars. Zhang et al.³⁰ analyzed the weakening technology of residual pillars in close range multi seam goaf mining, evaluating stress disturbance from residual pillars on underlying extraction and outlining floor stress distribution before and after pillar unloading. Wang et al.³¹ studied overburden behavior in fully mechanized faces, identifying instability mechanisms of coal pillars under thick direct roofs and proposing control techniques for middle and lower layered sections.

In recent years, because of the development of microseismic monitoring technology, the application of this monitoring to warn of the manifestation of rock burst and dynamic disaster characteristics in mining areas and tunnels, and to obtain the location of overburden fractures, has become a commonly used monitoring method in major mines^{32,33}. Monitoring results provide a valuable basis for numerical simulations and mechanical analysis, facilitating in-depth investigation of disasters induced by overlying rock fractures³⁴. In this regard, Cui et al.^{35,36} studied rock burst mechanisms associated with gently inclined roof failure. By integrating microseismic monitoring with 3DEC numerical simulations, they analyzed the fracture behavior of key strata and the evolution of overburden structures during mining. Their findings offer technical support for early warning and prevention of rock bursts under similar conditions.

Due to the significant differences in geological and overburden rock characteristics in close distance coal seams mining, and the varying mechanisms of interlayer rock fractures, research in this area still needs to be continuously strengthened. The paper focuses on the strong mining pressure manifestation caused by the breaking of interlayer hard rock in the close distance coal seams mining of Kuangou Mine. Stemmed from microseismic monitoring and numerical simulation results, the evolution process of interlayer hard rock strata under two seams mining is analyzed. At the same time, a cantilever beam structure model of interlayer hard rock strata influenced by residual coal pillar is established to analyze parameters such as deflection, rotation angle, and elastic energy under the critical breaking state of interlayer rock strata, and to form the relationship between the total energy of interlayer rock strata breaking and the cantilever structure and inverted trapezoidal overburden. Based on this, the pressure reduction and prevention measures for slicing mining were developed, providing a guarantee for the safety production of the mine.

Analysis of the disaster characteristics caused by overburden fracture

Kuangou Mine mainly mines the B2 and B4-1 coal seams, both of which have an average inclination angle of 14°. There are thick and hard sandstone layers between the coal seams.

The thickness of the B4-1 seam is 3 m. The thickness of the lower B2 seam is 9.5 m. In the B4-1 coal seam, there are mainly two working faces, W1143 and W1145. The B2 coal seam mainly includes two working faces, W1121 and W1123. The position relationship of the working face is shown in Fig. 1. To ensure safe mining, the upper B4-1 coal seam had been mined first, followed by the lower B2 coal seam. Thus, the mining sequence of the four working faces in the study zone is: W1143 → W1145 → W1121 → W1123. The mining of W1143 and W1145 working faces had been completed with the 5 m coal pillar remaining. The W1121 working face had been fully mined. Currently, the W1123 working face is being mined, with a 15 m coal pillar left. According to the mining deployment, the W1145 goaf is located above the W1123 working face, with a vertical height difference of 44 m between the two coal seams. In terms of direction, the horizontal projection of the W1145 goaf overlaps significantly with the local area of the W1123 working face.

Due to the difference in thickness between the B2 and B4-1 coal seams, the W1145 and W1143 working faces adopt the strike longwall mining method, while the W1121 and W1123 working faces adopt the fully-mechanized top coal caving mining method. Therefore, as the W1123 working face continues to be mined, some of its mining areas will gradually approach the goaf above, which will result in the superposition of mining disturbance stresses in the two coal seams. In addition, the influence of the residual coal pillar (5 m) in the B4 coal seam has led to significant mining pressure in W1123 working face. In this case, it is highly prone to energy shock caused by the rupture of hard rock layers in the mine.

Microseismic monitoring has become a widely adopted technique in recent years for assessing the stability and energy release characteristics of surrounding rock in major mines. This method involves deploying sensors within the rock to capture elastic waves generated by rock fractures due to mining-induced disturbances. These signals are used to locate microseismic events in time and space and to estimate their magnitudes. Based on principles of seismology, the source mechanisms are inferred through analysis of P-wave and S-wave characteristics, enabling the interpretation of stress field changes and the assessment of potential geotechnical hazards. Such analyses provide a scientific basis for early warning of mining-related dynamic disasters. In light of the specific problems faced in the mining area examined, we utilizes an ARAMIS microseismic monitoring system to record energy events occurring between 620 m and 770 m during the mining of the W1123 working face.

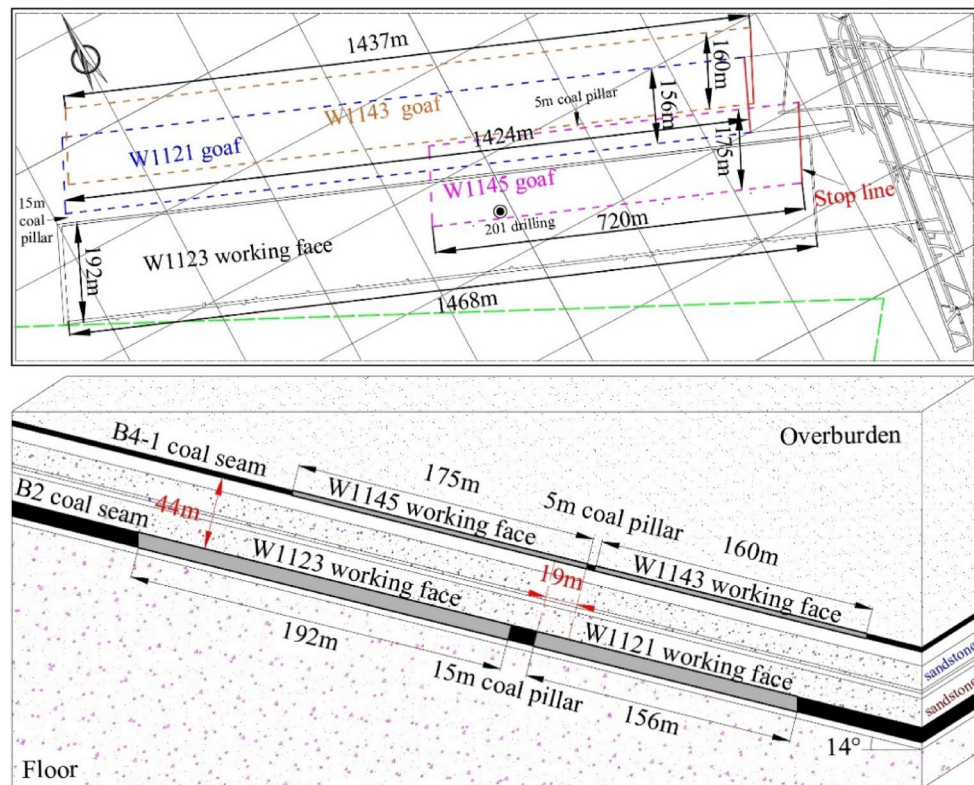


Fig. 1. Relationship diagram of B2 and B4-1 coal seams: (A) Working faces layout plan, (B) Layout plan of working face section.

According to the requirements for instrument use and the mining situation, all microseismic events are classified into levels I to V based on their energy levels. The energy discrimination standard for level I microseismic events is $0-10^3$ J, for level II microseismic events it is 10^3-10^4 J, for level III it is 10^4-10^5 J, for level IV it is 10^5-10^6 J, and for level V it is 10^6-10^7 J. From the perspectives of the location and characteristics of the disaster causing events, this paper analyzes the causes of the disaster after the overburden rock fracture in two coal seams mining.

Determination of prone zones for disaster events caused by gently inclined close distance coal seams mining

According to Fig. 2, microseismic events of magnitude III and IV are mainly distributed in a zigzag pattern along the edge of the W1145 goaf; The V-level high-energy events are mainly distributed in the 15 m coal pillar and its surrounding tunnels. From a vertical perspective, the distribution of III-V level microseismic events mainly occurs in the interlayer hard rock layers above the 15 m coal pillar, while V level events frequently occur below the 5 m coal pillar in B2 coal seams. Especially when the stope advanced 719 m, the maximum energy event during the monitoring period occurred, with an energy of 4.2×10^6 J. At this time, a rock burst occurred in the 15 m coal pillar within a range of 50 m ahead of the stope, accompanied by a loud sound. After the sound was detected, it was found that there was a clear phenomenon of fragmentation at the bottom corner of the roadway around the coal pillar. Overall, as the B4-1 coal seam goaf approaches, microseismic events at all levels will occur more frequently around the hard interlayer rock layers, indicating that the overburden of W1123 working face is gradually disturbed by the dual mining. The interlayer rock layers will continuously accumulate elastic properties and eventually break and release energy.

Energy characteristics analysis of microseismic events

By analyzing all the microseismic events that occurred during the mining of the W1123 working face from 620 m to 770 m, it is known that a total of 28,785 microseismic events were monitored, with a total energy of 1.758×10^8 J and an average single event energy value of 6110 J. Among them, the number of grade I and II microseismic events ($<10^3$ J) was huge, reaching 28,097, accounting for 98% of the total events, but their total energy accounted for only 27%, indicating that the occurrence of such events is a signal of the continuous expansion and development of internal joints and fractures in coal and rock under mining disturbance; However, there were only 673 microseismic events with magnitude III and IV, but the energy accounted for 34%. It can be seen that the frequent occurrence of such events means that the stress in the coal rock is concentrated, and the coal rock structure is gradually deteriorating; Finally, although there were only 15 V-level high-energy events (10^6-10^7 J), their energy proportion reached 42.85%. The occurrence of such events indicates the sudden release

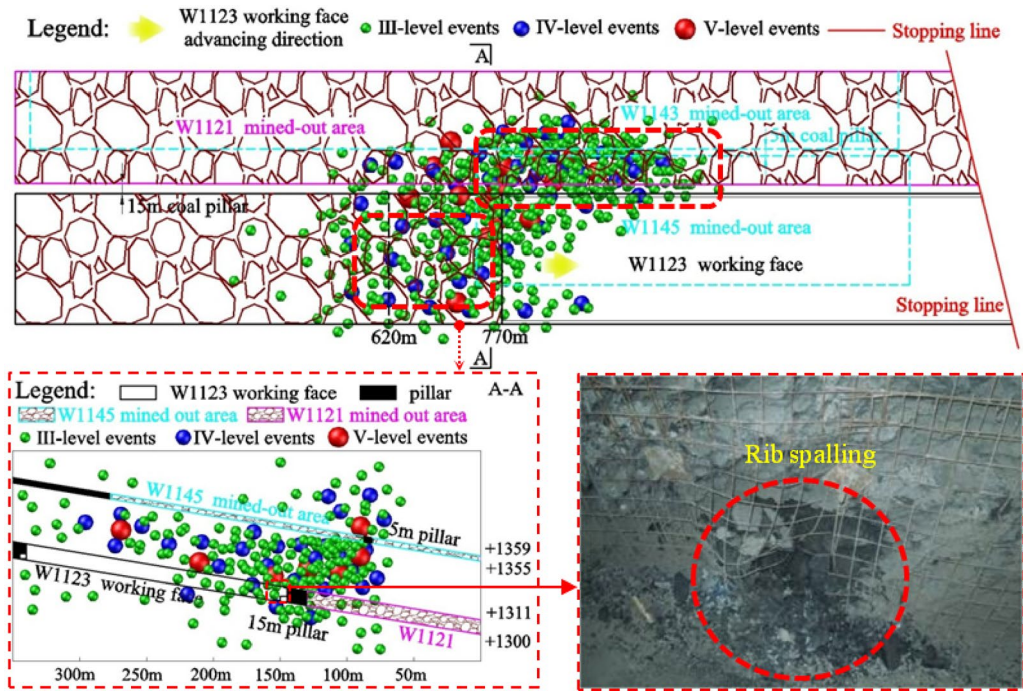


Fig. 2. Hypocentral location of III- V level microseismic events in range of 620–770 m.

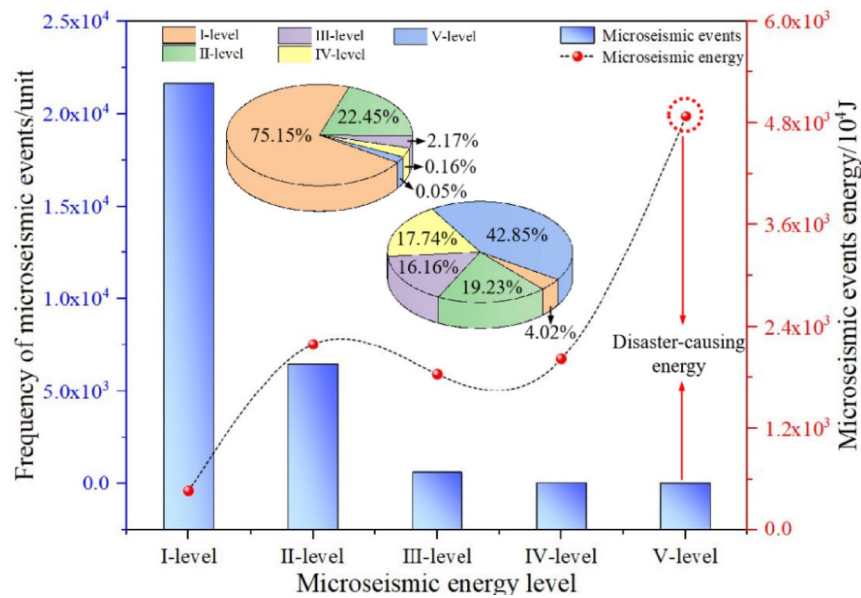


Fig. 3. The characteristics of microseismic events of different energy levels.

of energy from coal rock accumulation, often resulting in significant mining pressure manifestations (as shown in Fig. 3; Table 1).

Finally, by analyzing the relevance between the position of the stope and the microseismic energy and number of events, it can be found from Fig. 4 that as the mining zone of W1123 stope gradually approaches or is located below the W1145 goaf, the microseismic energy and number of events show a gradually increasing trend. This indicates that under the combined action of residual coal pillar in the upper part and multiple mining disturbances in the stope, the interlayer hard rock layers in the upper part of B2 coal seam will gradually accumulate high energy until they reach the threshold for energy release, which is also the main cause of disaster. Once a V-level high-energy event (10^6 - 10^7 J) occurs, there is often a noticeable manifestation of mining pressure. Combined with the occurrence location and distribution pattern of high-energy microseismic events, it can be

Microseismic events	Energy level	Number of events	Average energy per individual event	Proportion of total events	Total energy per level event	Energy proportion
I-level	$0-10^3$ J	21,633	212 J	75.15%	4.58×10^6 J	4.02%
II-level	10^3-10^4 J	6464	3400 J	22.45%	2.19×10^7 J	19.23%
III-level	10^4-10^5 J	626	2.95×10^4 J	2.17%	1.84×10^7 J	16.16%
IV-level	10^5-10^6 J	47	4.3×10^5 J	0.16%	2.02×10^7 J	17.74%
V-level	10^6-10^7 J	15	3.25×10^6 J	0.0521%	4.88×10^7 J	42.85%

Table 1. Characteristics of energy levels to total microseismic events.

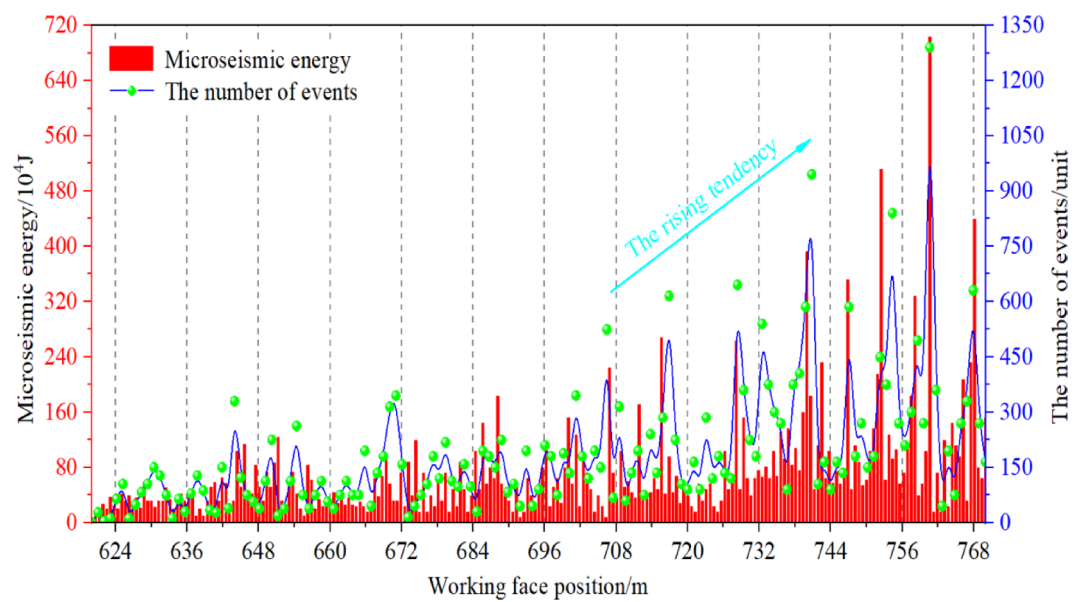


Fig. 4. Distribution characteristics of microseismic events during the 620–770 m mining of W1123 working face.

found that the instability and fracture of interlayer hard rock will directly affect the safe of the entire W1123 stope.

Numerical simulation of the fracture process of interlayer hard rock after close distance coal seams mining

On site microseismic monitoring found that interlayer rock are the main location where disasters occur in the mine. To further analyze the migration law of overburden and the fracture of interlayer hard rock, we used 3DEC (3-Dimensional Distinction Element Code) software (version DP 5.20, developed by Itasca Consulting Group, Inc.) based on Discrete Element Method (DEM) for numerical simulation analysis. This software can explicitly simulate the mechanical behavior of rock block systems cut by discrete joint networks, and is particularly adept at dealing with large deformation and failure problems in discontinuous media. These numerical simulation works could provide a foundation for the subsequent construction of mechanical models.

Construction of discrete element numerical model

The construction of the model relies on the rock occurrence characteristics and historical mining situation of Kuangou Mine. The inclination angle between the B2 and B4-1 coal seams simulated by the model is 14° , with a coal seam spacing of 44 m. The size of the model simulated by the model is $520 \text{ m} \times 10 \text{ m} \times 400 \text{ m}$. The width of the coal pillar in the W1123 working face section simulated by the model is 15 m, and the residual coal pillar width in the B4-1 coal seam is 5 m. The Mohr Coulomb criterion built into the simulation software is selected as the constitutive model. Subsequently, displacement constraints are applied to both sides and the bottom of the model, with no limit on the top displacement.

Apply a vertical load of 2.5 MPa at the top to ensure that the coal seam coverage is consistent with the site. This simulation strictly follows the on-site mining sequence, starting with B4-1 coal seam (W1143 and W1145 working face), and then the B2 coal seam (W1121 working face), to analyze the overburden rock structure evolution under close range coal seams mining. The constructed numerical calculation model is shown in Fig. 5.

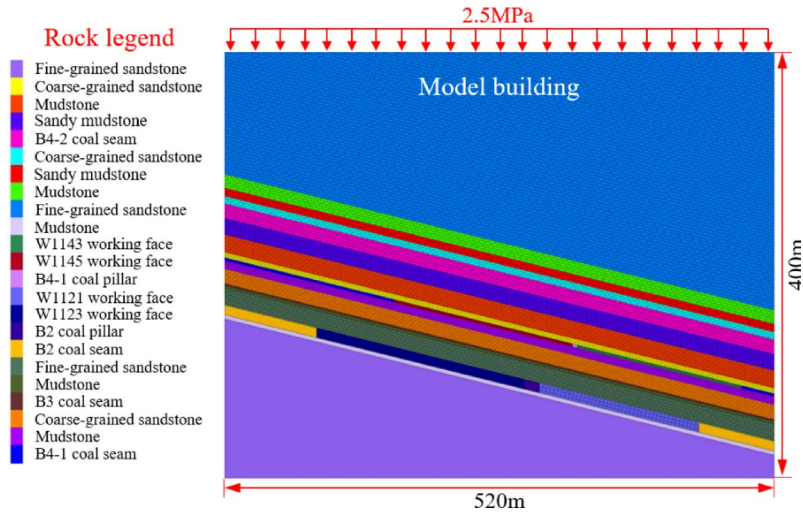


Fig. 5. Numerical calculation model of close distance coal seams mining.

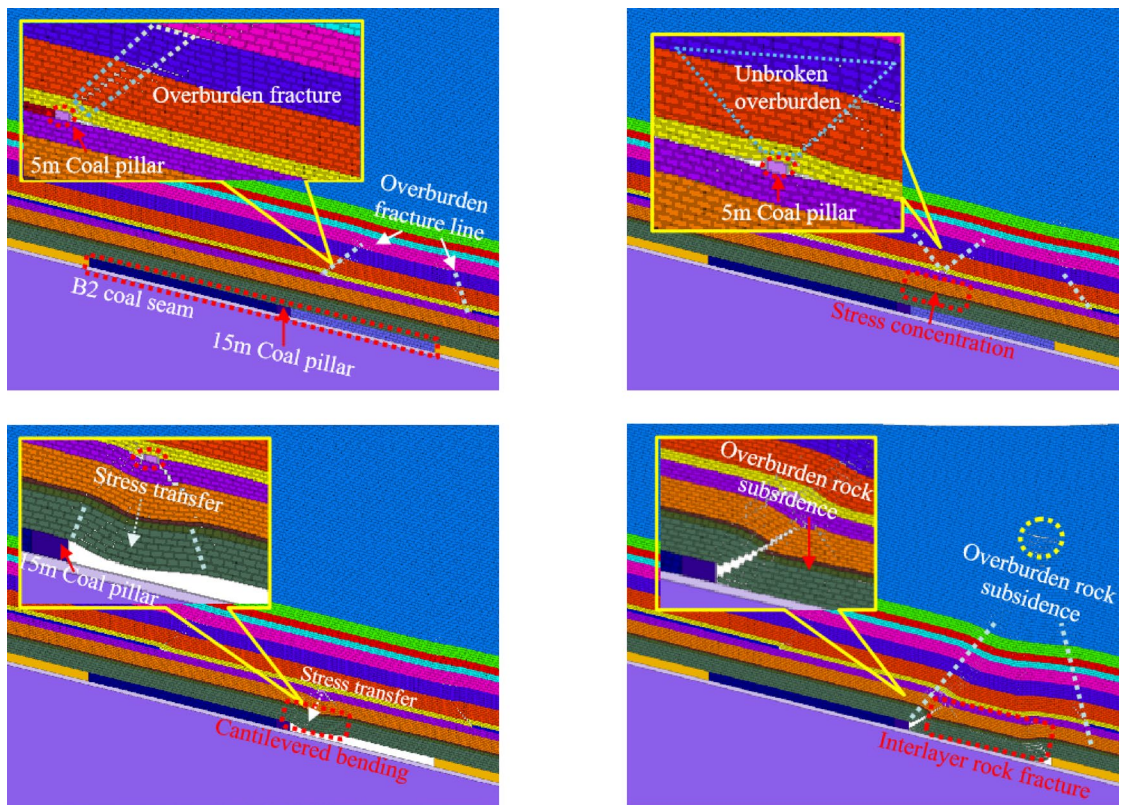


Fig. 6. Fracture morphology of overburden under disturbance during close distance coal seam mining: (A) W1143 excavation to balance, (B) W1145 excavation to balance, (C) W1121 excavation for 3000 steps, (D) W1121 excavation to balance.

Analysis of fracture morphology and displacement characteristics of interlayer hard rock

Figure 6 shows the fracture morphology of the overburden under the disturbance of mining in B4-1 and B2 coal seams. According to Fig. 6A and B, due to the mining of B4-1 coal seam, the upper rock layer of B2 coal seam has collapsed to a certain extent. Because of the presence of 5 m residual coal pillar, the overburden rock is relatively intact and distributed in an inverted ladder shape, and there are obvious overburden fracture lines on both sides of the pillar. According to Fig. 6C and D, it can be seen that as the excavation of the W1121 working face in the B2 coal seam reaches equilibrium, there is a large range of overburden rock movement on the right side of the entire model. Compared with the mining situation of the W1143 working face in the upper part, the

range of overburden rock fracture lines that have already appeared is significantly larger, extending to the blue area, and the cracks generated by the overburden rock fracture are wider. In addition, the inverted trapezoidal overburden rock carried by the residual coal pillar in the B4-1 coal seam significantly affects the deflection of the interlayer rock layers. At this time, the interlayer rock layers near the 15 m coal pillar side show obvious bending and eventually form a fracture, which triggers the subsidence and migration of the entire overburden rock. In addition, there is a hanging phenomenon of interlayer rock layers on the right side of the 15 m coal pillar, and a small triangular separation zone appears in the lower part. The overburden rock fracture line on the 15 m coal pillar continues to extend upwards, eventually connecting with the fracture line formed by mining, resulting in a large-scale subsidence on the right side of the entire model.

Figure 7 shows the distribution characteristics of the displacement field of the overburden rock under the disturbance of mining in B4-1 and B2 coal seams. From Fig. 7A and B, it can be seen that with the two working faces mining of B4-1 coal seam, the overburden rock of the B4-1 coal seam exhibit a large-scale migration phenomenon, but the migration amount is relatively small, fluctuating between 1.75 and 3.2 m, as shown in the grass green area extending to the surface in Fig. 7B. From Fig. 7C and D, it can be seen that when the excavation calculation of the W1121 working face reaches equilibrium, the interlayer rock and their overlying rocks show significant subsidence. This can be seen in the red orange triangular area of Fig. 7D. At this time, it can be found that the 5 m coal pillar left in the B4-1 coal seam has already undergone unstable subsidence, resulting in a hump shaped displacement peak area around the 15 m section of the coal pillar in the W1123 working face.

Based on the fracture morphology of interlayer hard rock and the overall characteristics of overburden rock migration, it can be concluded that the 5 m residual coal pillar of B4-1 coal seam are the main cause of the fracture of the lower interlayer hard rock, and the inverted trapezoidal overburden structure is the key to the occurrence of this overburden rock migration process. In addition, with the breaking and collapse of interlayer rock, this inverted trapezoidal overlying rock structure will also experience overall subsidence and eventually collide with the B2 coal seam floor, which is also one of the sources of high-energy events in previous microseismic monitoring.

Mechanism of interlayer hard rock fracture and analysis of disaster energy

Mechanical analysis of interlayer hard rock with loading to fracture

In microseismic monitoring and numerical simulation, it can be found that as the interlayer hard rock is affected by multiple mining disturbances, the cantilever structure formed by mining will be directly affected by the residual coal pillar. Therefore, the unbroken trapezoidal overburden load on the residual coal pillar is the main force source for the bending of the hanging rock layer. As the W1121 or W1123 working face advances through

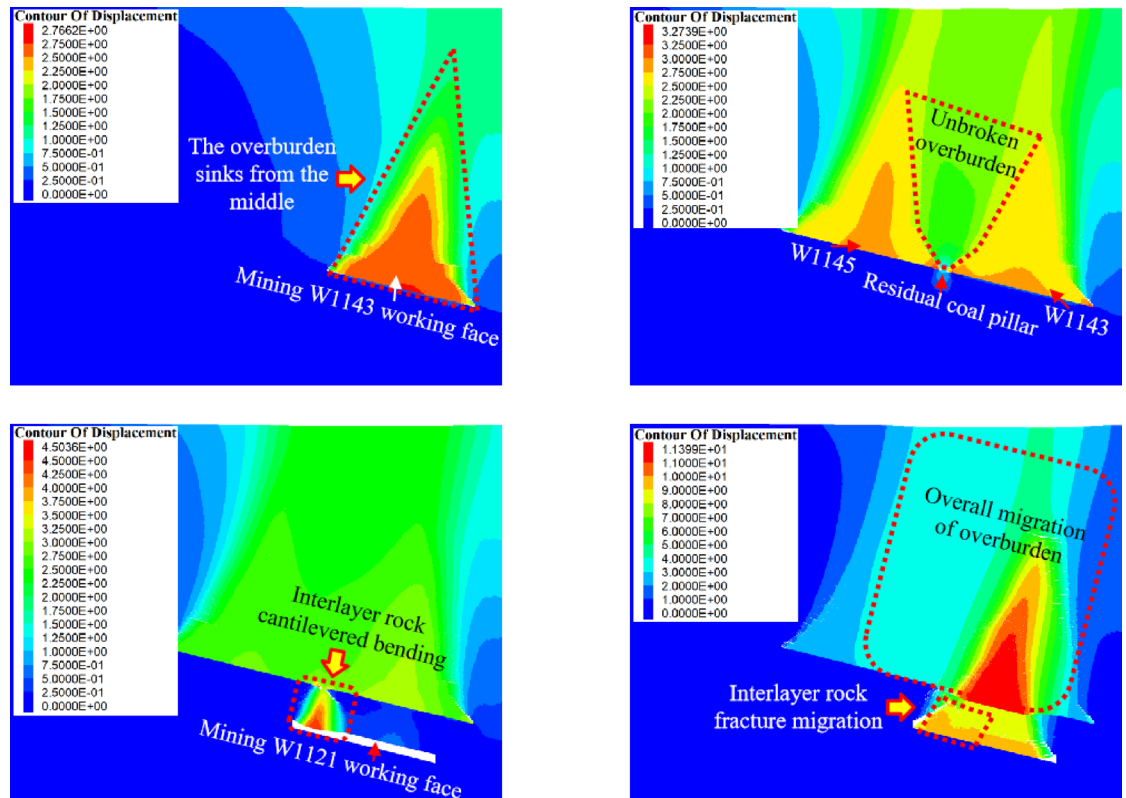


Fig. 7. Deformation characteristics of overburden during close distance coal seams mining: (A) W1143 excavation to balance, (B) W1145 excavation to balance, (C) W1121 excavation for 3000 steps, (D) W1121 excavation to balance.

the goaf of the B4-1 coal seam, the hard rock layers between the layers undergo flexural fracture, leading to the overall subsidence of the inverted trapezoidal overlying rock. In this dynamic instability process, the fracture of the cantilever rock layer will release a lot of elastic energy accumulated due to stress concentration, while the sinking of the upper trapezoidal overburden will release gravitational potential energy and collide with the bottom plate. Due to the close release time of elastic energy and gravitational potential energy, the surrounding roadways and coal pillar are prone to dynamic disasters. Therefore, conducting mechanical analysis of interlayer hard rock fracture is the key to obtaining the disaster mechanism. The loading characteristics of the rock can be shown in Fig. 8.

As shown on the right side of Fig. 8, the paper simplifies the load characteristics of interlayer strata and forms a cantilever structure model of interlayer strata for gently inclined coal seams. To simplify the calculation, a Cartesian coordinate system is established with pivot point O as the coordinate origin. From this, it can be seen that this cantilever structure is mainly subjected to the combined effects of its self weight stress G in the y -axis component, the overlying load Q supported by the residual coal pillar in the upper coal seam in the y -axis component, and the force F_1 of the broken overlying rock structure formed by the mining disturbance of W1145 working face on the cantilever beam. On this basis, Eqs. (1)–(3) can be obtained, and the load on the cantilever beam can be simplified to obtain Eqs. (4) and (5).

$$G = G_0 + G_1 \tag{1}$$

$$G_0 = \gamma_0 h_0 (l - l_1) z \tag{2}$$

$$G_1 = \gamma_0 h_0 l_1 z \tag{3}$$

$$q_0 = \frac{F_1 + G_0}{l - l_1} \cos \alpha \tag{4}$$

$$q_1 = \frac{Q + G_1}{l_1} \cos \alpha \tag{5}$$

In the equations, G is the gravity of the cantilever beam, kN; G_0 is the gravity of the x -direction $(0, l - l_1)$ section of the cantilever beam, kN; G_1 is the gravity of the x -direction $(l - l_1, l)$ section of the cantilever beam, kN; l is the critical breaking length of the cantilever beam, m; l_1 is the length of the bottom rock layer of the inverted trapezoidal overlying rock, m; F_1 is the force of the broken overlying rock on the cantilever beam in the W1145 goaf, kN; Q is the load of the inverted trapezoidal overlying rock supported by the residual coal pillar in the upper coal seam, kN; q_0 is the y -direction uniformly distributed load of the simplified cantilever beam in the $(0, l - l_1)$ section, MPa; q_1 is the y -direction uniformly distributed load of the simplified cantilever beam in the $(l - l_1, l)$ segment, MPa; h_0 is the thickness of the cantilever rock layer, m; γ_0 is the bulk density of the cantilever rock layer, kN/m^3 ; z is the depth in the z -direction of the coordinate system, m.

Using the cross-sectional method again, the moment $M(x)$ of any cross-section of the cantilever beam under local concentrated stress can be obtained from Eqs. (4) and (5):

$$M(x) = \frac{q_0}{2} x^2 + (q_0 l_1 - q_1 l_1 - q_0 l) x + \left[\frac{q_0}{2} l^2 + (q_0 - q_1) \frac{l_1^2}{2} + (q_1 - q_0) l_1 l \right] \tag{6}$$

On this basis, the deflection curve equation of the cantilever beam can be formed:

$$\omega''(x) = \frac{M(x)}{EI} \tag{7}$$

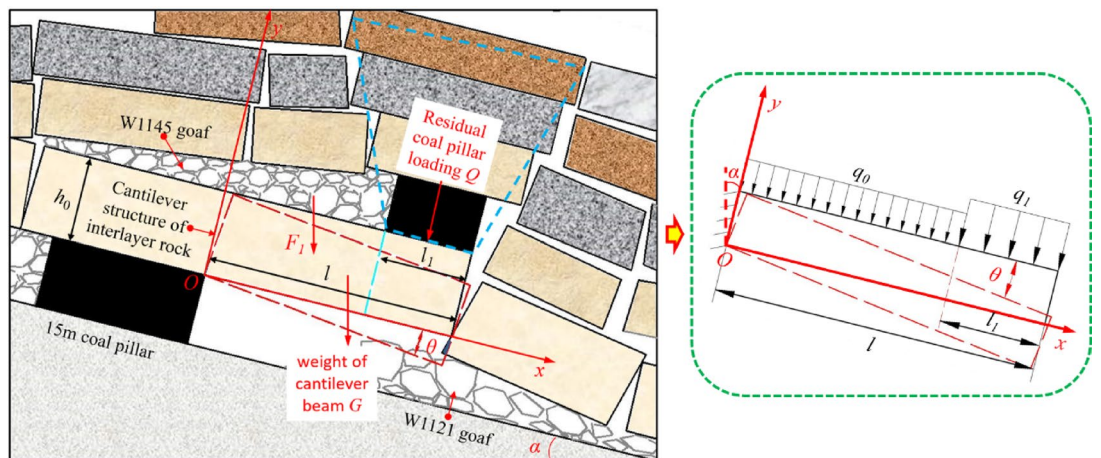


Fig. 8. Schematic diagram of interlayer loading mechanics model.

In the equation, EI represents the bending stiffness of the cantilever beam, $\text{kN}\cdot\text{m}^2$.

Integrating Eqs. (6) and (7) together yields l :

$$EI\omega'(x) = EI\theta = \frac{q_0}{6}x^3 + \frac{q_0l_1 - q_1l_1 - q_0l}{2}x^2 + \left[\frac{q_0}{2}l^2 + (q_0 - q_1)\frac{l_1^2}{2} + (q_1 - q_0)l_1l\right]x + C_1 \quad (8)$$

$$EI\omega(x) = \frac{q_0}{24}x^4 + \frac{q_0l_1 - q_1l_1 - q_0l}{6}x^3 + \left[\frac{q_0}{4}l^2 + \frac{q_0 - q_1}{4}l_1^2 + \frac{q_1 - q_0}{2}l_1l\right]x^2 + C_1x + C_2 \quad (9)$$

In the equations, $\omega(x)$ is the deflection at a certain point of the cantilever beam; θ is the ultimate rotation angle of the cantilever beam, $^\circ$. Substituting the boundary conditions, if the deflection and rotation angle at the fulcrum O of the cantilever beam are both 0, it means that when $x=0$, $\theta_0=0$, $\omega(0)=0$. By substituting into Eqs. (8) and (9), it can be concluded that both C_1 and C_2 are 0. From this, we can obtain the deflection curve equation and the rotation angle equation:

$$\omega(x) = \frac{q_0}{24EI}x^4 + \frac{q_0l_1 - q_1l_1 - q_0l}{6EI}x^3 + \left[\frac{q_0}{2}l^2 + \frac{q_0 - q_1}{2}l_1^2 + (q_1 - q_0)l_1l\right]\frac{x^2}{2EI} \quad (10)$$

$$\theta(x) = \frac{q_0}{6EI}x^3 + \frac{q_0l_1 - q_1l_1 - q_0l}{2EI}x^2 + \left[\frac{q_0}{2}l^2 + \frac{q_0 - q_1}{2}l_1^2 + (q_1 - q_0)l_1l\right]\frac{x}{EI} \quad (11)$$

When $x=l$, the deflection of the cantilever beam is maximum. Substituting it into Eq. (10), we can obtain:

$$\omega_{\max} = \frac{q_0}{8EI}l^4 + \frac{q_1 - q_0}{3EI}l_1l^3 + \frac{q_0 - q_1}{4EI}l_1^2l^2 \quad (12)$$

The maximum moment of the cantilever beam occurs at its critical fracture position, that is, when $x=0$. Substituting it into Eq. (6), we can obtain:

$$M_{\max} = \frac{q_0}{2}l^2 + (q_0 - q_1)\frac{l_1^2}{2} + (q_1 - q_0)l_1l \quad (13)$$

Among them, q_1 and q_0 in Eq. (13) can be substituted according to Eqs. (4) and (5). To avoid redundancy, only explanation is provided here.

On this basis, by combining the bending strain energy equation inside the cantilever beam and substituting the maximum moment M_{\max} , the elastic energy released by the fracture of the cantilever beam can be obtained:

$$V_{\text{et}} = \frac{M_{\max}^2 l}{2EI} \quad (14)$$

In the equation, V_{et} is the elastic energy released by the fracture of the cantilever beam, J .

Analysis of inverted trapezoidal overburden upper the residual coal pillar

As previously analyzed, the mining of B4-1 coal seam resulted in broken overburden on both sides of the residual coal pillar, causing the overlying strata of the coal pillar to be distributed in an inverted ladder shape. Among them, under the influence of coal seam dip angle, the side with a larger overburden fracture angle is often located at the upper end of the coal pillar, while the overburden fracture angle at the lower end of the coal pillar is often relatively smaller. For the determination of the overburden load, the calculation of the inverted trapezoidal overburden structure can be simplified, as shown in Fig. 9.

Assuming the total thickness of the inverted trapezoidal overlying rock is h , the left overlying rock fracture angle caused by the mining disturbance of W1123 is η , and the right overlying rock fracture angle caused by the mining disturbance of W1145 is β , the inverted trapezoidal overburden has n layers, counted as the 1st to n layers, and the height of the i th layer is h_i . Since its lowest layer (assumed to be the 1st layer) is connected to the end of the cantilever beam, the length of the bottom of the lowest layer is the length from the end of the cantilever beam to the cutting of W1145, which is l_1 . Therefore, it is assumed that the length of the bottom of the second layer is l_2 , the length of the bottom of the n th layer is l_n , and the bottom of the latter layer is exactly the top of the previous layer. The length of the top layer is l_{n+1} , from which we can obtain:

$$h = h_1 + h_2 + \dots + h_n \quad (15)$$

$$l_2 = l_1 + \frac{h_1}{\tan(\eta - \alpha)} + \frac{h_1}{\tan(\beta + \alpha)} = l_1 + h_1 \frac{\tan(\eta - \alpha) + \tan(\beta + \alpha)}{\tan(\eta - \alpha)\tan(\beta + \alpha)} \quad (16)$$

$$l_3 = l_2 + h_2 \frac{\tan(\eta - \alpha) + \tan(\beta + \alpha)}{\tan(\eta - \alpha)\tan(\beta + \alpha)} = l_1 + \frac{\tan(\eta - \alpha) + \tan(\beta + \alpha)}{\tan(\eta - \alpha)\tan(\beta + \alpha)}(h_1 + h_2) \quad (17)$$

$$l_{n+1} = l_1 + \frac{\tan(\eta - \alpha) + \tan(\beta + \alpha)}{\tan(\eta - \alpha)\tan(\beta + \alpha)}(h_1 + h_2 + \dots + h_n) \quad (18)$$

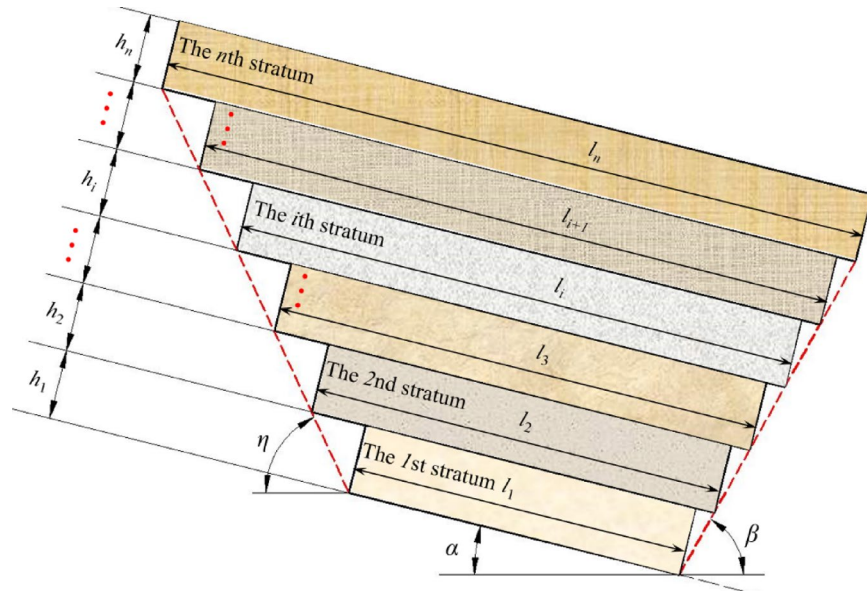


Fig. 9. Overburden inverted trapezoidal rock stratum structure.

On this basis, assuming that the unit bulk density of each rock layer is $\gamma_1, \gamma_2, \dots, \gamma_n$, the gravity load of each layer can be obtained, that is:

$$Q_1 = \gamma_1 h_1 \frac{l_1 + l_2}{2} = \gamma_1 h_1 z \left[l_1 + \frac{\tan(\eta - \alpha) + \tan(\beta + \alpha)}{\tan(\eta - \alpha) \tan(\beta + \alpha)} h_1 \right] \quad (19)$$

$$Q_2 = \gamma_2 h_2 \frac{l_2 + l_3}{2} = \gamma_2 h_2 z \left[l_1 + \frac{\tan(\eta - \alpha) + \tan(\beta + \alpha)}{\tan(\eta - \alpha) \tan(\beta + \alpha)} \left(h_1 + \frac{h_2}{2} \right) \right] \quad (20)$$

$$Q_n = \gamma_n h_n \frac{l_n + l_{n+1}}{2} = \gamma_n h_n z \left[l_1 + \frac{\tan(\eta - \alpha) + \tan(\beta + \alpha)}{\tan(\eta - \alpha) \tan(\beta + \alpha)} \left(h_1 + \dots + h_{n-1} + \frac{h_n}{2} \right) \right] \quad (21)$$

From this, it can be concluded that under the influence of gravity, the load Q of the inverted trapezoidal overlying rock structure acting on the coal pillar is:

$$Q = Q_1 + \dots + Q_n = \sum_{i=1}^n \gamma_i h_i z \left[l_1 + \frac{\tan(\eta - \alpha) + \tan(\beta + \alpha)}{\tan(\eta - \alpha) \tan(\beta + \alpha)} \left(\sum_{k=1}^i h_k - \frac{h_i}{2} \right) \right] \quad (22)$$

By substituting it into Eq. (14), the final gravitational potential energy V_G generated by the sinking of the inverted trapezoidal overlying rock can be obtained as:

$$V_G = Q h_s z = h_s z \sum_{i=1}^n \gamma_i h_i z \left[l_1 + \frac{\tan(\eta - \alpha) + \tan(\beta + \alpha)}{\tan(\eta - \alpha) \tan(\beta + \alpha)} \left(\sum_{k=1}^i h_k - \frac{h_i}{2} \right) \right] \quad (23)$$

Therefore, based on the previous numerical simulation of the interlayer rock fracture process, it can be found that the elastic energy released by the cantilever beam fracture and the gravitational potential energy generated by the sinking of the inverted trapezoidal overlying rock due to the cantilever beam fracture are the main energy sources of the entire disaster process. Thus:

$$V = V_G + V_{et} = \frac{M_{\max}^2 l}{2EI} + h_s z \sum_{i=1}^n \gamma_i h_i z \left[l_1 + \frac{\tan(\eta - \alpha) + \tan(\beta + \alpha)}{\tan(\eta - \alpha) \tan(\beta + \alpha)} \left(\sum_{k=1}^i h_k - \frac{h_i}{2} \right) \right] \quad (24)$$

In the equation, V is the total disaster energy induced by the entire breaking process, J ; V_{et} is the elastic energy released by the cantilever beam breaking, J ; V_G is the gravitational potential energy generated by the sinking of the inverted trapezoidal overlying rock, J ; h_s is the sinking distance of the inverted trapezoidal overlying rock structure, m .

Analysis of the disaster mechanism caused by the fracture of interlayer rock

Through an analysis of the entire calculation process, it can be observed that key relationships—such as those between the bending deformation parameters (deflection ω , rotation angle θ), the ultimate moment M_{\max} , and the released elastic energy V_{et} during fracture—all incorporate three fundamental rock parameters: the length l of the cantilever beam, the loads q_0 and q_1 borne by the cantilever beam, and the bending resistance of the cantilever beam itself (bending stiffness EI). Thus, it can be concluded that:

Firstly, the formation of the cantilever beam structure within the interlayer hard rock stratum results from mining-induced disturbances in the B4-1 and B2 coal seams, which trigger a redistribution of the overburden structure. The overhanging length l of the beam increases progressively as the working face advances. By combining the critical deflection (Eq. (12)) and the elastic energy release expression (Eq. (14)), it can be seen that the length l of the cantilever beam is directly proportional to its ultimate deflection ω_{\max} and the released elastic energy V_{et} . This implies that a greater cantilever length leads to higher elastic energy accumulation and release during bending and failure.

Secondly, a greater weight of the inverted trapezoidal overlying rock results in higher elastic energy associated with disaster initiation in the cantilever structure. This is due to the product of the uniformly distributed loads q_0 and q_1 borne by the cantilever beam and its cantilever length l is the total load of the cantilever beam. Among these, the load Q from the unbroken overburden supported by the residual coal pillar serves as the primary force source and is entirely applied to the left segment l_1 of the cantilever. As indicated by Eq. (13), only when the gravitational force from the inverted trapezoidal overlying rock reaches a sufficient magnitude can the maximum moment M_{\max} be generated, leading to the bending and fracture of the cantilever beam.

Thus, the flexural capacity of the cantilever beam itself plays a decisive role in the amount of elastic energy released upon its failure. As indicated in Eq. (7), for a given ultimate deflection ω , a higher bending stiffness EI results in a greater ultimate moment M_{\max} that the beam can sustain, thereby enabling the accumulation of more elastic energy V_{et} . Consequently, the magnitude of disaster energy is intrinsically linked to the length and strength of the cantilever structure, as well as the weight of the overlying rock. The interplay of these three factors readily contributes to the initiation of dynamic disasters during the hanging and fracturing of hard rock layers in close-distance coal seam mining.

Weakening and cutting roof measures for interlayer hard rock

Based on the law of energy release caused by the breaking of hard rock layers between layers, it can be concluded that with the breaking of cantilever rock layers, a large amount of elastic energy accumulated due to stress concentration will be released, leading to the manifestation of dynamic disasters. Therefore, how to accelerate the breaking process of interlayer hard rock, weaken their lithological strength, and reduce the overhanging length of the rock is of great significance for pressure reduction and prevention. Due to the high-density and high-strength hard rock between the B2 and B4-1 coal seams in Kuangou Mine, only by using a combination of water injection weakening and roof cutting blasting measures can the integrity of the hard rock be destroyed³⁷, and the internal cracks and structural weak planes of the rock layer that need to be broken be rapidly expanded along the tangential direction of the blasting surface³⁸ while the axial strength of the interlayer hard rock is reduced³⁹. The ultimate goal is to weaken the degree of fracture and energy release of this rock layer, to achieve the goal of pressure reduction prevention and safe mining in the working face (in Fig. 10).

Firstly, water injection weakening drilling was carried out in the W1123 lower groove and blasting working roadway, with a drilling diameter of 100 mm, a hole depth of 50 m. The construction requirements for water injection weakening holes were to be arranged 45 m ahead of the W1123 stope, with a total of 6 sets of sections arranged, each with 3 holes. 2 holes were arranged in the W1123 lower groove (with drilling angles of 67.5° northwest to north and 22.5° respectively), and 1 hole was arranged in the blasting process roadway (with drilling angles of 67.5° northwest to north), with an interval of 10 m between adjacent sections. The drilling was

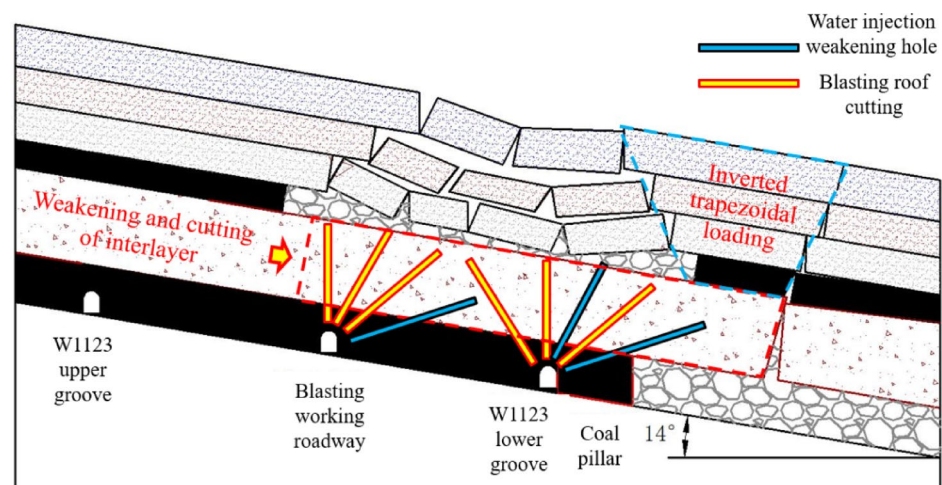


Fig. 10. Water injection weakening and blasting roof cutting borehole layout effect.

Order number	Angle (°)	Drilling length (m)	Charge length (m)	Explosive charge (kg)	Sealing length (m)	Detonator
Lower groove 1#	Northwest direction 45°	35	25	120	10	6
Lower groove 2#	North direction 0°	35	25	120	10	6
Lower groove 3#	Northeast direction 22.5°	35	25	120	10	6
Blasting roadway 1#	Northwest direction 67.5°	35	25	120	10	6
Blasting roadway 2#	Northwest direction 45°	35	25	120	10	6
Blasting roadway 3#	North direction 0°	35	25	120	10	6
Total		210	150	720	60	36

Table 2. Single group blasting hole parameters.

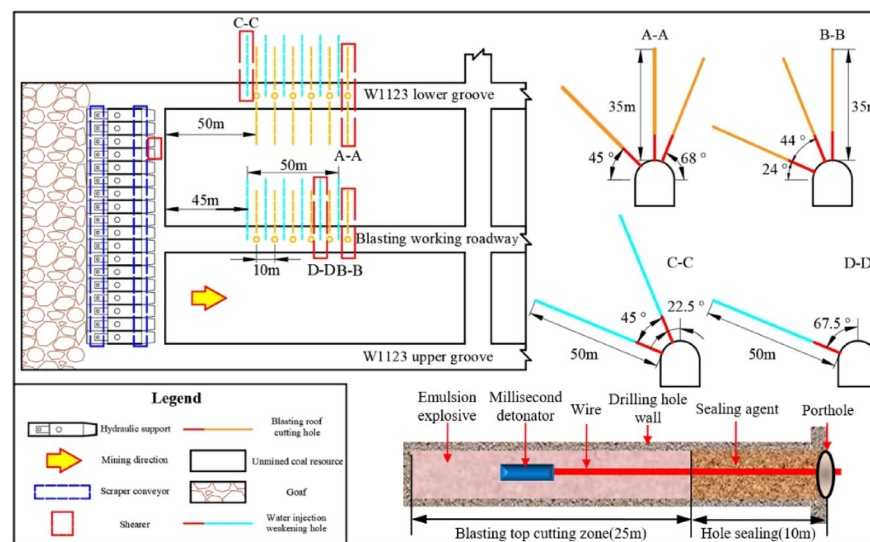


Fig. 11. Water injection weakening and blasting roof cutting process diagram.

carried out using the ZDY-4000 fully hydraulic tunnel drilling rig and its supporting drill pipe, and the borehole sealer was used in conjunction with cement sealing. The model of the pressurized water pump is BZW125/50 coal rock high-pressure water injection pump, with a rated flow rate of 125 L/min, a rated water injection pressure of 50 MPa, and a water injection time of 4–7 h or stopped when the roof of the roadway within 10 m before and after the water injection section is flooded.

Subsequently, blasting roof cutting holes were arranged 50 m ahead of the working face, and the construction position of the blasting boreholes was W1123 lower groove and blasting working roadway. A total of 6 sets of sections were arranged for blasting and roof cutting work, with 6 boreholes drilled for each Sect. 3 of them were in the W1123 groove and 3 were in the blasting process lane. The adjacent two sets of sections were spaced 10 m apart and distributed in a fan-shaped pattern. The drilling diameter is 100 mm, the hole depth is 35 m, and the No. 3 emulsion explosive is used for blasting. The diameter of the explosive is 90 mm, the charge length is 25 m, the sealing length is 10 m, and the forward charge is used with a charge density of 4.8 kg/m. The explosive charge for each borehole is 120 kg, and the total explosive charge for one blasting group is 720 kg. A single group requires 6 detonators. The blasting adopts a wire connection method, with parallel connections inside the holes, and one blasting hole detonates once. In addition, both water injection and blasting drilling are carried out using the ZDY-4000 fully hydraulic tunnel drilling rig. The blasting hole parameters are shown in Table 2.

The water injection weakening and blasting roof cutting process is shown in Fig. 11.

Monitoring and analysis of weakening and cutting roof effect

To verify the effectiveness of weakening and cutting roof measures, two methods of microseismic and acoustic emission (AE) monitoring were used to analyze the manifestation of mining pressure before and after the implementation of the measure. The entire microseismic monitoring process started 15 days before the control measures were taken and ended 15 days after the completion of the control measures. According to Fig. 12A, before taking roof prevention and control measures, there were significantly more microseismic energies and event numbers, with an average daily microseismic energy of 588×10^4 J and an average daily microseismic event number of 956. With the implementation of weakened roof cutting, the interlayer rock were cut off on the 16th day of the monitoring period. Afterwards, both microseismic energy and event count significantly decreased, with an average microseismic energy of 180×10^4 J, a decrease of 69.4% compared to before the implementation

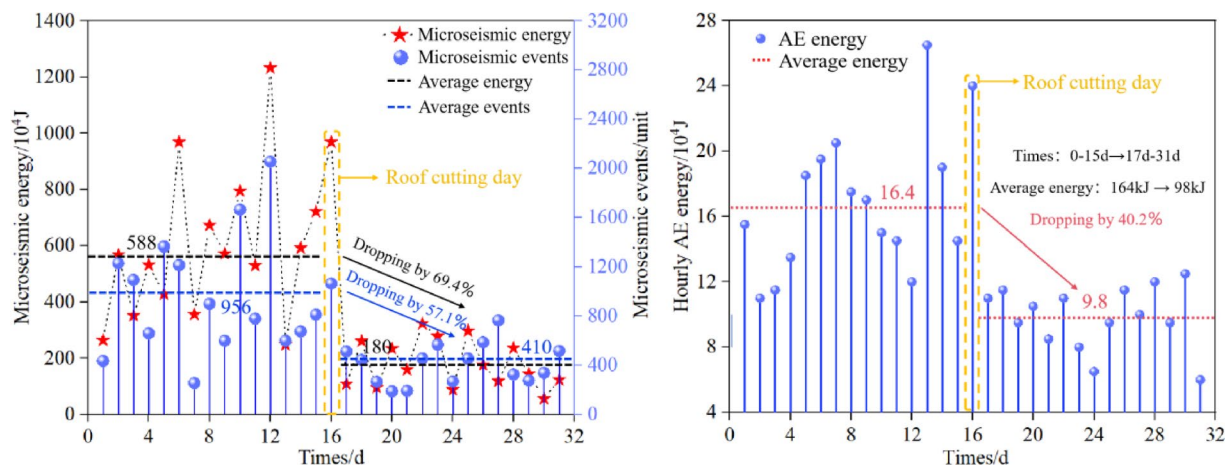


Fig. 12. Analysis of weakening and cutting roof effect: (A) Microseismic monitoring, (B) AE monitoring.

of the measures; The average number of microseismic events was 410, a decrease of 57.1% compared to before the implementation of the measures.

From Fig. 12B, it can be seen that the hourly energy of AE was relatively high 15 days before the implementation of prevention and control measures, with an average energy of 16.4×10^4 J and a large fluctuation amplitude. After the completion of the measures, the AE energy significantly decreased and the fluctuation amplitude also decreased. Among them, the average hourly energy of AE during the monitoring period of 17–31 days was 9.8×10^4 J, a decrease of 40.2% compared to 0–15 days.

By analyzing the above monitoring results, it can be concluded that before these control measures are taken, the interlayer hard rock will gradually accumulate and release a large amount of elastic properties. With the adoption of these measures, the integrity of coal and rock masses can be effectively destroyed, their energy storage capacity can be reduced, the danger of large-scale overhanging of interlayer rock can be eliminated, and the elastic performance of the rock layer can be smoothly released, providing a guarantee for the safe mining of gently inclined close distance coal seams.

Conclusions

1. The mechanism of interlayer hard rock fracture in gently inclined close-distance coal seam mining is attributed to the failure of its cantilever structure and the overall subsidence of the overburden. This process evolves through three stages: energy accumulation within the intact overlying strata, critical fracture of the hard rock cantilever, and energy release resulting from interlayer rock failure. Medium- energy to high-energy microseismic events observed during this process are distributed in a zigzag pattern along the perimeter of the W1145 goaf in the horizontal direction, and are concentrated within the interlayer hard rock above the 15 m coal pillar in the vertical direction.
2. A mechanical model of the interlayer rock cantilever beam was established based on the fracture process in interlayer hard rock. The deflection curve and rotation angle equation at the critical fracture state were derived, and the relationship between the released elastic energy and the overlying load and structural configuration was quantified. The gravitational load characteristics of the inverted trapezoidal overburden were analyzed, leading to an integrated model relating the total energy released during interlayer fracture to both the cantilever geometry and the overburden load. The results indicate that a heavier trapezoidal overburden exerts greater energy loading on the cantilever structure. Longer cantilever lengths correlate with higher accumulated elastic energy, while greater structural stiffness enhances energy storage capacity. The interaction of these factors readily induces dynamic disasters during interlayer hard rock failure in close-distance mining.
3. Based on the energy release mechanism of interlayer hard rock failure, it is concluded that mitigating disaster risks requires weakening the lithology of the hard rock and reducing the cantilever length. Corresponding control strategies, such as water injection for weakening and blasting for roof cutting, were proposed. These measures effectively expand primary fractures and structural planes in the target rock, reduce its axial strength, and compromise its integrity. Implementation has significantly reduced large-scale roof hanging events, achieving mine pressure relief and disaster prevention objectives. This approach provides a technical reference for layered mining under similar conditions.

Data availability

The datasets generated and/or analysed during the current study are not publicly available due to requirement of confidentiality, but are available from the corresponding author on reasonable request.

Received: 28 July 2025; Accepted: 9 October 2025

Published online: 17 November 2025

References

- Xie, H. P. et al. Development opportunities of the coal industry towards the goal of carbon neutrality. *J. China Coal Soc.* **46**, 2197–2211 (2021).
- Zhang, Y. et al. Research on coal-rock identification method and data augmentation algorithm of comprehensive working face based on FL-Segformer. *Int. J. Coal Sci. Technol.* **11**, 48 (2024).
- Lei, W. L. et al. Research on stress release and pressure relief mechanism of underlying coal and rock under protective layer mining. *Sci. Rep.-UK.* **15**, 5583 (2025).
- Chen, Y. et al. State-of-the-art on the anchorage performance of rock bolts subjected to shear load. *Int. J. Coal Sci. Technol.* **11**, 9 (2024).
- Zhou, J. L. et al. Mechanism and prevention of coal bursts in gob-side roadway floor under Thick and hard roof in the deep mining area of Ordos. *Int. J. Coal Sci. Technol.* **11**, 80 (2024).
- Du, X. H. et al. Damage and energy characteristics of coal rock combinations with inclined coal seams under axial loading. *Sci. Rep.-UK.* **14**, 21881 (2024).
- Dai, L. P. et al. Parameter design method for destressing boreholes to mitigate roadway coal bursts: theory and verification. *Rock. Mech. Rock. Eng.* **57**, 9539–9556 (2024).
- Qiao, G. D. et al. Theoretical analysis and engineering application of controllable shock wave technology for enhancing coalbed methane in soft and low-permeability coal seams. *Int. J. Coal Sci. Technol.* **11**, 25 (2024).
- Long, H. et al. Thermal-hydraulic-mechanical coupling analysis of N2-ECBM recovery efficiency: pressure and temperature dependence. *Energy* **233**, 121179 (2021).
- Liu, Y. L. et al. Risk assessment of disaster chain in multi-seam mining beneath gully topography. *Int. J. Disast Risk Re.* **111**, 104750 (2024).
- Yang, K. et al. Evolution of mining-induced stress in downward mining of short-distance multiseam. *Geofluids* **2022**, 3305734 (2022).
- Mu, H. W. et al. Regional local integrated rockburst monitoring and early warning for multi-seam mining. *J. Geophys. Eng.* **18**, 725–739 (2021).
- Mu, H. W. et al. Investigation of strong strata behaviors in the close-distance multiseam coal pillar mining. *Shock Vib.* **2021**, 1263275 (2021).
- Khan, M. et al. Predicting deformation kinetics and fractures propagation in coal-rock masses using acoustic emission testing. *Int. J. Coal Sci. Technol.* **12**, 28 (2025).
- Jia, C. et al. Mining pressure distribution law and disaster prevention of isolated Island working face under the condition of hard umbrella arch. *Rock. Mech. Rock. Eng.* **57**, 8323–8341 (2024).
- Du, X. H. et al. Coal damage and energy characteristics during shallow mining to deep mining. *Energy* **291**, 130375 (2024).
- Zhong, T. et al. Mechanism of rock burst vertical damage induced by layered crack structures of the steeply inclined extremely Thick coal seams. *Int. J. Coal Sci. Technol.* **12**, 24 (2025).
- Lai, X. P. et al. Research on the mechanism of rockburst induced by mined coal-rock linkage of sharply inclined coal seams. *Int. J. Min. Met. Mater.* **31**, 929–942 (2024).
- Lai, X. P. et al. Research on mechanism and control of floor heave of mining-influenced roadway in top coal caving working face. *Energies* **13**, 381 (2020).
- Xu, H. C. et al. Energy dissipation characteristics and shock mechanism of coal-rock mass induced in steeply-inclined mining: comparison based on physical simulation and numerical calculation. *Acta Geotech.* **18**, 843–864 (2023).
- Yu, X. Y. et al. Mining mode of layered and coordinated disaster reduction in Thick coal seam of Barapukuria coal mine in Bangladesh. *J. China Coal Soc.* **47**, 2352–2359 (2022).
- Yu, X. Y. et al. Development law of water-conducting fracture zone in overlying rock with layered mining under strong water-bearing body in Barapukuria coal mine. *J. China Coal Soc.* **47**, 29–38 (2022).
- Zhang, J. X. et al. Disaster-causing mechanism of extremely Thick igneous rock induced by mining and prevention method by backfill mining. *Eur. J. Environ. Civ. Eng.* **24**, 307–320 (2020).
- Zhang, J. X. et al. Risk assessment and prevention of surface subsidence in deep multiple coal seam mining under dense above-ground buildings: case study. *Hum. Ecol. Risk Assess.* **25**, 1579–1593 (2019).
- Deng, X. J. et al. Strata behavior in extra-thick coal seam mining with upward slicing backfilling technology. *Int. J. Min. Sci. Technol.* **26**, 587–592 (2016).
- Huang, Q. X. et al. Coupling control on pillar stress concentration and surface cracks in shallow multi-seam mining. *Int. J. Min. Sci. Technol.* **31**, 95–101 (2021).
- Huang, Q. X. et al. Experimental investigation on crack development characteristics in shallow coal seam mining in China. *Energies* **12**, 1302 (2019).
- Huang, Q. X. et al. Research on overburden movement characteristics of large mining height working face in shallow buried thin bedrock. *Energies* **12**, 4208 (2019).
- Peng, R. et al. Evaluating the safety of using the combined mining method in close-distance coal seams. *Geotech. Geol. Eng.* **42**, 1063–1087 (2024).
- Zhang, J. et al. Study on the coal pillar weakening technology in close distance multi-coal seam Goaf. *Energies* **15**, 6532 (2022).
- Wang, Z. Q. et al. Instability mechanism and control of section coal pillar in fully mechanized mining face with super Thick roof and extra Thick seam. *J. China Coal Soc.* **46**, 3756–3770 (2021).
- Liu, F. et al. Applications of microseismic monitoring technique in coal mines: A state-of-the-art review. *Appl. Sci.* **14**, 1509 (2024).
- Chen, J. et al. A quantitative pre-warning for coal burst hazardous zones in a deep coal mine based on the spatio-temporal forecast of microseismic events. *Process. Saf. Environ.* **159**, 1105–1112 (2022).
- Wang, S. W. et al. Mechanism of rockburst induced by the microseismic event in the floor strata of high tectonic stress zones: A case study. *Int. J. Coal Sci. Technol.* **11**, 76 (2024).
- Cui, F. et al. Study on the law of fracture evolution under repeated mining of close-distance coal seams. *Energies* **13**, 6064 (2020).
- Cui, F. et al. Study on the fracture law of inclined hard roof and surrounding rock control of mining roadway in Longwall mining face. *Energies* **13**, 5344 (2020).
- Kang, H. P. et al. Case study of hydraulic fracturing for coal burst risk mitigation. *Int. J. Coal Sci. Technol.* **12**, 1–15 (2025).
- Hao, Q. et al. Numerical investigation on damage effect of deep hole pre-cracking roof rock and controlling rockburst. *Int. J. Coal Sci. Technol.* **12**, 62 (2025).
- Chen, H. Y. et al. Experimental study on damage law of coal seam under hydraulic fracturing and blast load. *Int. J. Coal Sci. Technol.* **12**, 1–16 (2025).

Acknowledgements

Thanks to funds supported by the National Natural Science Foundation of China (Grant No. 52264007), the Gansu Province Youth Science and Technology Fund Program (Grant No. 24JRRM026 and 25JRRM016), the

Key R&D Program Project of Qingyang City (Grant No. QY-STK-2024B-190), the Youth Doctoral Support Project for Universities in Gansu Province (Grant No. 2025QB-093), the Postdoctoral Research Funding in Shaanxi Province (Grant No. 2024BSHYDZZ017), Yulin Science and Technology Plan Project (Grant No. 2024-CXY-164), and Longdong University Industry-University Collaboration Horizontal Research Project (HXZK2451).

Author contributions

X.Y.: Conceptualisation, software, writing—original draft preparation, prepared Figs. 2, 3, 6, 8, 9. X.D.: Software, writing—original draft preparation, prepared Figs. 5 and 7. P.S.: Software, data curation, writing—editing, prepared Figs. 1 and 4. L.Y.: Method, data curation, prepared Fig. 12. W.L.: Writing—reviewing and editing, prepared Fig. 10. W.Y.: Writing—reviewing, prepared Fig. 11. Z.Z.: Writing—reviewing and editing.

Funding

This study was funded by the National Natural Science Foundation of China (Grant No. 52264007 and 52564023), the Gansu Province Youth Science and Technology Fund Program (Grant No. 24JRRM026 and 25JRRM016), the Key R&D Program Project of Qingyang City (Grant No. QY-STK-2024B-189 and QY-STK-2024B-190), the Youth Doctoral Support Project for Universities in Gansu Province (Grant No. 2025QB-093), the Gansu Provincial Education Science and Technology Innovation Project (2025 A-202), the Longdong University Doctoral Fund (XYBYZK2405), the Postdoctoral Research Funding in Shaanxi Province (Grant No. 2024BSHYDZZ017), Yulin Science and Technology Plan Project (Grant No. 2024-CXY-164), and Longdong University Industry-University Collaboration Horizontal Research Project (HXZK2451).

Declarations

Competing interests

The authors declare no competing interests.

Additional information

Correspondence and requests for materials should be addressed to X.Y.

Reprints and permissions information is available at www.nature.com/reprints.

Publisher's note Springer Nature remains neutral with regard to jurisdictional claims in published maps and institutional affiliations.

Open Access This article is licensed under a Creative Commons Attribution-NonCommercial-NoDerivatives 4.0 International License, which permits any non-commercial use, sharing, distribution and reproduction in any medium or format, as long as you give appropriate credit to the original author(s) and the source, provide a link to the Creative Commons licence, and indicate if you modified the licensed material. You do not have permission under this licence to share adapted material derived from this article or parts of it. The images or other third party material in this article are included in the article's Creative Commons licence, unless indicated otherwise in a credit line to the material. If material is not included in the article's Creative Commons licence and your intended use is not permitted by statutory regulation or exceeds the permitted use, you will need to obtain permission directly from the copyright holder. To view a copy of this licence, visit <http://creativecommons.org/licenses/by-nc-nd/4.0/>.

© The Author(s) 2025